Experimental observation of thermalisation with noncommuting charges

Florian Kranzl,^{1, 2, *} Aleksander Lasek,³ Manoj K. Joshi,¹ Amir Kalev,⁴ Rainer Blatt,^{1, 2} Christian F. Roos,^{1, 2, †} and Nicole Yunger Halpern^{3, 5, 6, 7, ‡}

¹Institut für Quantenoptik und Quanteninformation,
Österreichische Akademie der Wissenschaften, Technikerstraße 21a, 6020 Innsbruck, Austria
²Institut für Experimentalphysik, Universität Innsbruck, Technikerstraße 25, 6020 Innsbruck, Austria
³Joint Center for Quantum Information and Computer Science,
NIST and University of Maryland, College Park, MD 20742, USA
⁴Information Sciences Institute, University of Southern California, Arlington, VA 22203, USA
⁵Institute for Physical Science and Technology, University of Maryland, College Park, MD 20742, USA
⁶ITAMP, Harvard-Smithsonian Center for Astrophysics, Cambridge, MA 02138, USA
⁷Department of Physics, Harvard University, Cambridge, MA 02138, USA
(Dated: February 11, 2022)

Quantum simulators have recently enabled experimental observations of quantum many-body systems' internal thermalisation. Often, the global energy and particle number are conserved, and the system is prepared with a well-defined particle number—in a microcanonical subspace. However, quantum evolution can also conserve quantities, or charges, that fail to commute with each other. Noncommuting charges have recently emerged as a subfield at the intersection of quantum thermodynamics and quantum information. Until now, this subfield has remained theoretical. We initiate the experimental testing of its predictions, with a trapped-ion simulator. We prepare 6–15 spins in an approximate microcanonical subspace, a generalisation of the microcanonical subspace for accommodating noncommuting charges, which cannot necessarily have well-defined nontrivial values simultaneously. We simulate a Heisenberg evolution using laser-induced entangling interactions and collective spin rotations. The noncommuting charges are the three spin components. We find that small subsystems equilibrate to near a recently predicted non-Abelian thermal state. This work bridges quantum many-body simulators to the quantum thermodynamics of noncommuting charges, whose predictions can now be tested.

INTRODUCTION

Two disparate, but conceptually kindred, fields have advanced rapidly over the past few years. In many-body physics, quantum simulators have grown to tens or even hundreds of particles [1–7] that can be indvidually controlled and measured [8, 9]. Experiments have elucidated how closed quantum many-body systems thermalise internally [10–12]. Typically, the evolutions conserve no quantities (as in gate-based evolutions), conserve energy (in quantum simulators), or conserve energy and particle number (in nonphotonic systems).

Separately, the subdiscipline of noncommuting charges has been emerging within quantum thermodynamics [13, 14], a subject grounded in foundational and information theory. Throughout thermodynamics, a system of interest \mathcal{S} exchanges quantities—particles, magnetization, etc.—with an environment \mathcal{E} . As \mathcal{S} has far fewer degrees of freedom than \mathcal{E} , we call \mathcal{S} "the small system" for short. As the quantities are conserved globally, we call them charges. Quantum charges are represented by Hermitian operators $Q_{\gamma=1,2,\dots,c}$, which are implicitly assumed to commute with each other in common thermodynamic arguments [15–21]. Yet noncommuting operators under-

lie quantum physics from uncertainty relations to measurement disturbance. What happens if thermodynamic charges fail to commute with each other? Whether \mathcal{S} can even thermalise is not obvious, as derivations of the thermal state's form implicitly rely on charges' commutation [18, 19, 22]. Recently, the study of noncommuting charges has swept across quantum thermodynamics [17–46]. Results have primarily been information-theoretic, although forays into many-body theory have begun recently [22, 27, 32–36, 43].

Several questions about noncommuting thermodynamic charges have been debated during the past few years. Information-theoretic arguments suggest that S equilibrates to near the *non-Abelian thermal state* (NATS) [15, 18–21],

$$\rho_{\text{NATS}} := \exp\left(-\beta \left[H - \sum_{\gamma=1}^{c} \mu_{\gamma} Q_{\gamma}\right]\right) / Z_{\text{NATS}} . \quad (1)$$

 β denotes the inverse temperature, H denotes the Hamiltonian of \mathcal{S} , the μ_{γ} denote effective chemical potentials, the Q_{γ} denote the c non-energy charges of \mathcal{S} , and the partition function Z_{NATS} normalises the state. States of the form (1) are called also generalised Gibbs ensembles, especially in the absence of noncommutation and the presence of integrability [47–49]. If the charges fail to commute, arguments for Eq. (1) rely on kinematics and idealisations, such as a very large \mathcal{SE} composite. Whether \mathcal{S} thermalises outside these idealisations, under realistic dynamics, has remained unclear, although [22]

^{*} The first two coauthors contributed equally.

 $^{^{\}dagger}$ christian.roos@uibk.ac.at

[‡] nicoleyh@umd.edu

presented numerical evidence that S does.

Whether experimentalists can observe ρ_{NATS} has remained even unclearer: Suppose that \mathcal{SE} is a closed quantum many-body system, as in many recent quantum-thermalisation experiments. Experimental control is finite. Any of the many charges may leak out of the ideally isolated \mathcal{SE} , breaking the conservation laws.

Another open question is the *extent* to which S thermalises, even ideally. Recall typical arguments for thermalisation in quantum many-body systems: The dynamics conserve at most one global charge, $Q_1^{\rm tot}$, apart from the energy—often, the particle number. \mathcal{SE} begins in a Q_1^{tot} sector and in a narrow energy window—in a microcanonical subspace. But suppose that the dynamics conserve multiple charges $Q_{\gamma=1,2,\ldots,c}^{\text{tot}}$ that do not all commute with each other. Due to the noncommutation, the charges share no eigenbasis, so they may share no eigenspace: They cannot necessarily have well-defined values simultaneously; no microcanonical subspace necessarily exists. Microcanonical subspaces have been generalised to approximate microcanonical (AMC) subspaces, to accommodate noncommuting charges [19]: In an AMC subspace, every $Q_{\gamma}^{\rm tot}$ has a fairly well-defined value. The uncertainty in the global charges' initial values has been conjectured to generate uncertainty in the long-time state of S: S may remain a little farther from ρ_{NATS} than it would remain from the relevant thermal state if the charges commuted [22].

We provide answers—some complete and some partial—to these and other open questions, by uniting the fields of quantum simulators and noncommuting thermodynamic charges. Using a quantum simulator of 9-15 trapped ions, we implement the experimental proposal in [22]. Each ion's two electronic states forms a qubit. We initialise the qubits in an AMC subspace. The evolution—an effective long-range Heisenberg coupling—conserves all the global-spin components $S_{x,y,z}^{\text{tot}}$. We experimentally implement the evolution by interspersing a long-range Ising coupling with global rotations and dynamical-decoupling sequences. Trotterisation of Heisenberg dynamics has been proposed theoretically [50, 51], realised experimentally in toy examples [52, 53], and used very recently to explore many-body physics in ensembles of Rydberg atoms [54, 55]. Here, we demonstrate its effectiveness in many-body experiments with trapped ions. Two nearest-neighbour ions form the system of interest, and the other ions form an effective environment (Fig. 1). We find that \mathcal{S} thermalises to near ρ_{NATS} , on average over copies of \mathcal{S} [15, 18–21]. The long-time distance to ρ_{NATS} is consistent with a bound predicted in [19]. Furthermore, we observe the thermalisation process in what is, to our knowledge, the first study of noncommuting charges' influence on thermalisation dynamics. To begin to isolate the noncommutation's effects, we compare our experiment with an evolution that conserves just commuting charges, S_z^{tot} and the energy. We observe that \mathcal{S} remains farther from the thermal state if the charges fail to commute. This

observation is consistent with the conjecture that noncommuting charges hinder thermalisation [19], as well as with the expectation that, in finite-size global systems, resistance to thermalisation grows with the number of charges [56, 57]. Our experiment offers a particularly quantum counterpart to the landmark experiment [58], in which a hitherto-unobserved equilibrium state was observed but the quantum physics of charges' noncommutation was left unexplored. The present work opens the emerging subfield of noncommuting thermodynamic charges to experiments.

RESULTS

We begin by explaining the experimental setup and initial state. We then observe the dynamics of thermalisation influenced by noncommuting charges, observe thermalisation to near ρ_{NATS} , and compare with thermalisation in the presence of two commuting charges.

Experimental setup

We perform the experiment on a trapped-ion quantum simulator [8]. A linear string of N=6–15 $^{40}\mathrm{Ca}^+$ ions is confined in a linear Paul trap (Fig. 1a). Let $\sigma_{\gamma}=\frac{2}{\hbar}S_{\gamma}$ denote the Pauli- γ operator, for $\gamma=x,y,z$. Let $|\gamma\pm\rangle$ denote the ± 1 eigenstates of σ_{γ} . We denote by $\sigma_{\gamma}^{(j)}$ the site-j Pauli operators; and, by $\sigma_{\gamma}^{\mathrm{tot}}$, the whole-chain operators. Each ion encodes a qubit in the Zeeman states $4^2\mathrm{D}_{5/2}$ and $4^2\mathrm{S}_{1/2}$, of respective magnetic quantum numbers m=5/2 and 1/2. We denote the states by $|z+\rangle$ and $|z-\rangle$. A pair of nearest-neighbour qubits forms the small system of interest; the remaining qubits form the environment.

We employ two types of coherent operations using a laser at 729 nm, which drives the quadrupole transition that connects the qubit states: (i) Denoting a rotated Pauli operator by $\sigma_{\phi}^{(j)} = \cos\phi\,\sigma_x^{(j)} + \sin\phi\,\sigma_y^{(j)}$, we perform global qubit rotations $U(\theta,\phi) = \exp(-i\frac{\theta}{2}\sum_{j=1}^N\sigma_{\phi}^{(j)})$. (ii) The effective long-range x-type Ising Hamiltonian

$$H_{xx} := \sum_{i \le k} \frac{J_0}{|j - k|^{\alpha}} \, \sigma_x^{(j)} \sigma_x^{(k)} \tag{2}$$

entangles qubits. We effect H_{xx} by off-resonantly coupling to the lower and upper vibrational sideband transitions of the ion strings' transverse collective modes [59]. Combining these two ingredients, we Trotterapproximate the Heisenberg Hamiltonian

$$H_{\text{Heis}} := \sum_{j < k} \frac{J_0}{3|j - k|^{\alpha}} \left(\sigma_x^{(j)} \sigma_x^{(k)} + \sigma_y^{(j)} \sigma_y^{(k)} + \sigma_z^{(j)} \sigma_z^{(k)} \right),$$
(3)

as shown in Fig. 1b and the Methods. The 1/3 appears because the Ising coupling (2) is distributed across three

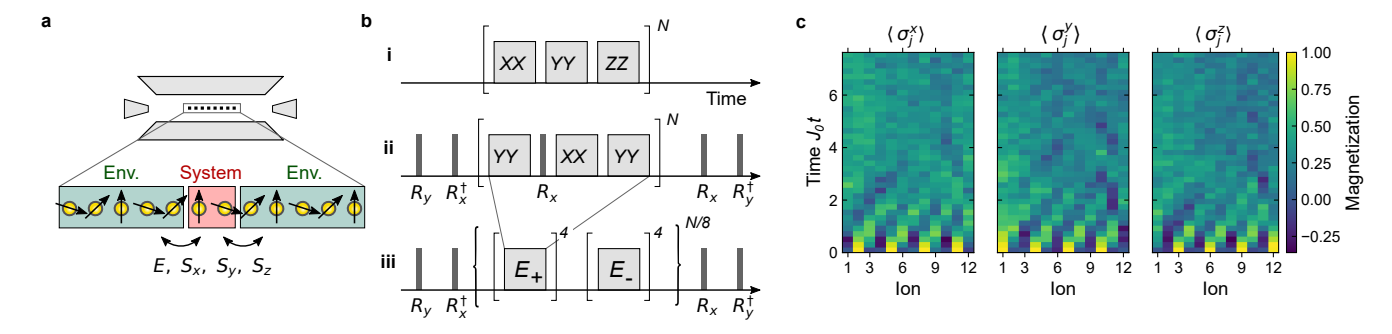


FIG. 1: Experimental setup and protocol: (a) A linear ion crystal of N=6–15 ions is trapped in a linear Paul trap. A small system exchanges charges (local instances of quantities that are conserved globally) with the surrounding environment: energy, E, and all components of angular momentum. (b) One can Trotter-approximate the Heisenberg evolution by consecutively evolving the state across short time steps under the three terms in the Hamiltonian (3). We experimentally realise two terms directly and generate the third using resonant $\pi/2$ -pulses (R_x and R_y). This pulse sequence further protects the state against dephasing noise (ii). Some of the building blocks E_+ are replaced with equivalent pulse sequences (E_-) to reduce pulse-length errors (iii). For further details, see the Methods. (c) Observed evolution of the initial state, $|y+,x+,z+\rangle^{\otimes 4}$, under the Trotter-approximated Heisenberg model (wherein $J_0=508$ rad/s and $\alpha=1.02$), when N=12. To present a complete picture of the dynamics, we derive the spin-excitation-hopping rate in App. A.

directions (x, y, and z). We implement a $\sigma_y^{(j)}\sigma_y^{(k)}$ coupling similarly, as described in the Methods. The pulse sequence was designed to realise H_{xx} while, via dynamical decoupling, mitigating dephasing and rotation errors.

At the beginning of each experimental trial, the ion string's transverse collective modes are cooled to near their motional ground state. Then, we prepare the qubits in the product state described in the next subsection. We then evolve the global system for a time t up to $J_0t_{\rm f}=(508~{\rm rad/s})\times(15~{\rm ms})\approx 7.6$ (Fig. 1c). The global system has largely equilibrated internally, and fluctuations are small, as shown two subsections below. Finally, we measure the states of all neighbouring qubit pairs (qubits 1 and 2, qubits 2 and 3, etc.) via quantum state tomography.

Initial state

Conventional thermalisation experiments begin with the global system in a microcanonical subspace. As our global charges do not all commute, they cannot have well-defined nonzero values simultaneously; no nontrivial microcanonical subspace exists. We therefore prepare the global system in an AMC subspace, where the charges have fairly well-defined values. We follow the proposal in [22] for extending the AMC subspace's definition, devised abstractly in [19], to realistic systems: In an AMC subspace, each global charge $Q_{\gamma}^{\rm tot}$ has a variance $\sim O([N]^{\nu})$, wherein $\nu \leq 1$. A product of single-qubit pure states meets this requirement [22].

We choose the tensor product to affirmatively answer an open question. In [22], ρ_{NATS} was found numerically to predict a small system's long-time state best. However, other thermal states approached ρ_{NATS} in accuracy as N grew. (Accuracy was quantified with the long-time

state's relative-entropy distance to a thermal state, as detailed below.) Does the NATS's accuracy remain greatest by a constant amount, as N grows, for any initial state? The answer is yes for all N realised in our experiment. App. B explains why the initial state,

$$|\psi_0\rangle := |y+, x+, z+\rangle^{\otimes N/3}, \tag{4}$$

consistently distinguishes the NATS. We also prove the following under assumptions met by our experiment in App. C: Consider averaging each thermal state over the global system. The average ρ_{NATS} differs from average competitor thermal states, as measured by nonzero relative-entropy distances. A constant lower-bounds the distances at all N, even in the thermodynamic limit (as $N \to \infty$). These empirical and analytical results establish the NATS as distinguishable even at large N.

The initial state determines the inverse temperature β and chemical potentials μ_{γ} in Eq. (1) [22]. Denote the global NATS by $\rho_{\mathrm{NATS}}^{\mathrm{tot}} := \exp\left(-\beta \left[H_{\mathrm{Heis}} - \sum_{\gamma=x,y,z} \mu_{\gamma} S_{\gamma}^{\mathrm{tot}}\right]\right)/Z_{\mathrm{NATS}}^{\mathrm{tot}}$, with $Z_{\mathrm{NATS}}^{\mathrm{tot}}$ defined to normalise the state. We define β and the μ_{γ} 's through

$$\langle \psi_0 | H_{\text{Heis}} | \psi_0 \rangle = \text{Tr} \left(H_{\text{Heis}} \, \rho_{\text{NATS}}^{\text{tot}} \right) \quad \text{and}$$
 (5)

$$\langle \psi_0 | \sigma_{\gamma}^{\text{tot}} | \psi_0 \rangle = \text{Tr} \left(\sigma_{\gamma}^{\text{tot}} \rho_{\text{NATS}}^{\text{tot}} \right) \quad \forall \gamma = x, y, z.$$
 (6)

We calculate the parameters numerically by solving a maximum-entropy problem, following [60, 61]: $\beta = -4.2 \times 10^{-4} \, \mathrm{s \, rad^{-1}}$, and $\mu_{x,y,z} = -307 \, \mathrm{rad \, s^{-1}}$.

Equilibration to near the non-Abelian thermal state

Figure 2 shows how accurately the NATS predicts a small system's state, as a function of time. The

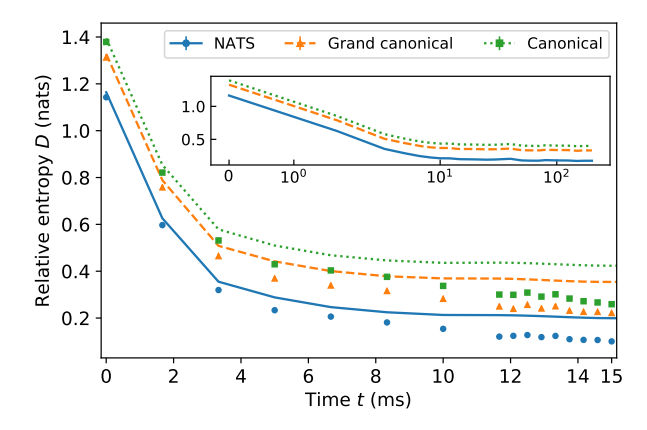


FIG. 2: Average distance from system-of-interest state to thermal prediction vs. time: The ion chain consists of N=12 qubits. Each nearest-neighbour pair forms a small system of interest. We measure its distance to the NATS (blue points), using the relative entropy [19], and average over the pairs in the chain. Markers show experimental data, while lines are calculated numerically from Eq. (3). Each data point is formed from 300 repetitions. The error bars, estimated by bootstrapping [62], are too small to see. Entropies are measured in units of nats (are base-e). We also compare the NATS prediction with two competitor thermal predictions, following [48, 58]: canonical and grand canonical states. At all times, the NATS predicts the state unambiguously more accurately than competitors do. The inset shows numerics up to 200 ms (on a log-scale axis). By 15 ms, the relative entropies have settled to near their long-term values, the inset shows.

global system size is N = 12. To construct the blue dots, we measure the time-dependent state $\rho_t^{(j,j+1)}$ of each nearest-neighbour qubit pair (j, j + 1), for j = $1, 2, \ldots, N-1$. We then calculate the state's relativeentropy distance to the NATS (defined below) [19]. In Eq. (1), H denotes the term in H_{Heis} [Eq. (3)] that acts nontrivially just on pair (j, j + 1). Following [19, 22], we measure the distance with the relative entropy: If χ and ξ denote quantum states (density operators) defined on the same Hilbert space, the relative entropy is $D(\chi||\xi) = \text{Tr}(\chi[\log \chi - \log \xi])$. All logarithms in this paper are base-e: Entropies are measured in units of nats (not to be confused with the NATS), rather than in bits. $D(\chi||\xi)$ quantifies the optimal efficiency with which the states can be distinguished, on average, in a binary hypothesis test. We average $D(\rho_t^{(j,j+1)}||\rho_{\text{NATS}})$ over the N-1 qubit pairs, producing $\langle D(\rho_t^{(j,j+1)}||\rho_{\text{NATS}})\rangle$. To our knowledge, this is the first report on the process of thermalisation colored by noncommuting charges (e.g., begun in an AMC subspace).

As in [48, 58], we compare the small system's state with competing predictions by other thermal states: the canonical state, $\rho_{\rm can}:=e^{-\beta H}/Z_{\rm can}$, and the grand canon-

ical state, $\rho_{\rm GC}:=\exp\left(-\beta\left\{H-\mu_zS_z^{(2)}\right\}\right)/Z_{\rm GC}$. The partition functions $Z_{\rm can}$ and $Z_{\rm GC}$ normalise the states. We denote by $S_z^{(2)}$ the total spin operator on two sites. We call $\rho_{\rm GC}$ "grand canonical" because S_z is equivalent to a spinless-fermion particle-number operator via a Jordan-Wigner transformation. As the blue discs (distances to $\rho_{\rm NATS}$) are lower than the orange triangles ($\rho_{\rm GC}$) and blue squares ($\rho_{\rm can}$), the NATS always predicts the state best.

The curves show results from numerical simulations. We calculate the global state's time evolution via direct multiplication with the Hamiltonian's sparse matrix representation. The experimental markers lie below the numerical curves, so the small system thermalises more in the experiment than theoretically. After all, the experimental ion chain is open and so has more opportunities to thermalise. By the same token, however, the ion chain can leak its four charges $(S_{x,y,z})$ and energy to the environment, violating the conservation laws ideally imposed on the ions. One might expect such a violation to prevent ρ_{NATS} from predicting the long-time state accurately. However, our results show that the chain is closed enough that no competitor thermal state, defined in terms of fewer charges, bests ρ_{NATS} as a prediction. The inset shows numerics until 200 ms. By $t_f = 15$ ms, the curves are approximately constant; the small system has approximately thermalised. Our choice of experimental run time is therefore justified. App. D contains further details about fluctuations of the relative entropy.

In Fig. 3, we fix $t_{\rm f}=15$ ms while varying the global system size. The blue discs represent the relative-entropy distance from the final system-of-interest state, $\rho_{\rm t_f}^{(j,j+1)}$, to the NATS, averaged over qubit pairs. The average distance declines from 0.2 nats to 0.12 nats as N grows from 6 to 15. For reference, $D(\chi||\xi)$ obeys no upper bound. We hence answer two open questions: Equilibration to near the NATS occurs in realistic systems and is experimentally observable, despite the opportunity for the spin chain to leak many charges via decoherence. Furthermore, the orange triangles (distances to $\rho_{\rm GC}$) lie 0.11 nats above the blue discs (distances to $\rho_{\rm Can}$) lie 0.16 nats above the blue discs, on average. Hence the NATS prediction is distinguishably most accurate at all N.

The red curve in Fig. 3 shows the best polynomial fit to the blue points (the distances to ρ_{NATS}), $0.42N^{-0.57}+0.02$. The fit was calculated via weighted least squares. For comparison, the bound predicted information-theoretically is $\langle D(\rho_{t_{\text{f}}}^{(j,j+1)}||\rho_{\text{NATS}})\rangle \leq (\text{positive constant})N^{-0.50}+(\text{positive constant})$ [19]. The experimental scaling exponent, -0.57, lies below the information-theoretic exponent, -0.50, and above the numerically predicted exponent, -2.448 [22]. Hence the experiment obeys the theoretical bound [19]. However, the experimental best-fit parameters have significant uncertainties (0.35, 1.58, and 0.32), being inferred from four data points.

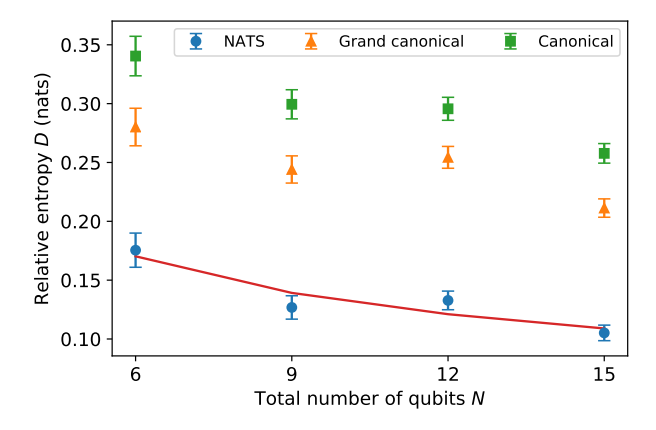


FIG. 3: Average distance from long-time system-of-interest state to thermal prediction vs. total number of qubits: Statistics are calculated as in Fig. 2. The NATS predicts the state most accurately at all system sizes. The best polynomial fit to the NATS data (red line) is $0.42N^{-0.57} + 0.02$. The scaling exponent -0.57 lies between the abstract theoretical prediction, -0.5 [19], and the numerical prediction, -2.448 [22].

We have observed equilibration to near the NATS, but the small system does not thermalise entirely: $\langle D(\rho_{t_f}^{(j,j+1)}||\rho_{\text{NATS}})\rangle \neq 0$. We expect the lingering athermality to stem partially from the global system's finite size [63, 64]. Yet charges' noncommutation has been conjectured to hinder thermalisation additionally [22]. We provide the first data about this conjecture, by comparing thermalisation steered by noncommuting charges with thermalisation steered by just commuting charges.

We realise the commuting case with the long-range XY Hamiltonian

$$H_{xy} := \sum_{j < k} \frac{1}{2} \frac{J_0}{|j - k|^{\alpha}} \left(\sigma_x^{(j)} \sigma_x^{(k)} + \sigma_y^{(j)} \sigma_y^{(k)} \right), \quad (7)$$

for N=12, with $J_0=508$ rad/s and $\alpha=1.02$ (see Methods for details). The charges are the total energy and $\sigma_z^{\rm tot}$. We Trotter-approximate H_{xy} similarly to $H_{\rm Heis}$ (App. E). After preparing $|y+,x+,z+\rangle^{\otimes N/3}$, we simulate H_{xy} for 10 ms.

Table I shows the results. The average small system thermalises more thoroughly when determined by commuting charges than when determined by noncommuting charges. For instance, in the commuting case, the relative entropy to $\rho_{\rm GC}$ descends as low as 0.070 nats, when N=15. In the noncommuting case, when N=15, the relative entropy to $\rho_{\rm NATS}$ reaches 0.105 > 0.070 nats. (The relative entropy is lower in the noncommuting case just when N=6, at the edge of a reasonable size for a global system in a thermalisation experiment.) This result is consistent with the conjecture that charges' noncommutation hinders thermalisation [22], as well as with the expectation that, in finite-size global systems, a small system's long-time entanglement entropy decreases as the

Number of qubits N	6	9	12	15
Relative entropy D	0.258	0.102	0.087	0.070
	± 0.016	$ \pm 0.008 $	± 0.007	± 0.006

TABLE I: Average distance from long-time system-of-interest state to grand canonical state when only energy and $\sigma_z^{\rm tot}$ conserved: Each nearest-neighbour pair in the ion chain forms a small system of interest. We measure its long-time state to the grand canonical state (the most accurate thermal prediction), using the relative entropy [19], measured in nats. Then, we average over the pairs in the chain. The average pair thermalises more thoroughly than if noncommuting charges are conserved, at all $N \geq 8$.

number of charges grows [57]. Future work will distinguish how much our charges' noncommutation is hindering thermalisation and how much the multiplicity of charges is.

CONCLUSIONS

We have observed the first experimental evidence of a particularly quantum equilibrium state: the non-Abelian thermal state, which depends on noncommuting conserved charges. Whereas typical many-body experiments begin in a microcanonical subspace, our experiment begins in an approximate microcanonical subspace. This generalisation accommodates the noncommuting charges' inability to have well-defined nontrivial values simultaneously. Our experiment affirmatively answers an open question: whether, for any initial state, the NATS remains a substantially better prediction than other thermal states as the global system grows. Our trapped-ion experiment affirmatively answers two more open questions: (i) whether realistic systems exhibit the thermodynamics of noncommuting charges and (ii) whether this thermodynamics can be observed experimentally, despite the multiplicity of conservation laws that decoherence can break. Our work therefore bridges quantum simulators to the emerging subfield of noncommuting charges in quantum-information-theoretic thermodynamics. The subfield has remained theoretical until now; hence many predictions now can, and should, be tested experimentally—predictions about reference frames, second laws of thermodynamics, information storage in dynamical fixed points, and more [17–46].

In addition to answering open questions, our results open avenues for future work. First, Fig. 3 contains a line of best fit whose scaling exponent lies near the theoretical prediction in [19]. However, the paucity of data points leads to a large experimental uncertainty. One can reduce the uncertainty by scaling up the system further. Similarly reducing the constant offset's uncertainty would provide evidence about another open question: whether

the small system thermalises fully as $N \to \infty$ [22]. A nonvanishing offset would suggest that noncommuting charges block thermalisation in the thermodynamic limit. Our offset, although positive, has too large an uncertainty for drawing conclusions.

Third, we observed that the small system thermalises less in the presence of noncommuting charges than in the presence of just commuting charges. This observation is consistent with the conjecture that charges' noncommutation may hinder thermalisation at all N [22]. Future study will tease apart effects of the charges' noncommutation from effects of the charges' multiplicity.

Finally, the quantum-simulation toolkit developed here merits application to other experiments. We combined our quantum simulator's native interaction with rotations and dynamical decoupling to simulate a nonnative Heisenberg interaction. The Trotterised longrange Hamiltonian, together with the single-qubit control used to initialise the system here, can be advantageous for studying more many-body physics with quantum simulators. These techniques can be leveraged to explore nonequilibrium Heisenberg dynamics [54, 55], topological excitations [65], and more.

METHODS

This section details the setup, the realisation of spinspin interactions, the Trotterisation of the Heisenberg Hamiltonian, and the quantum state tomography and statistical analysis.

Experimental setup

A linear ion crystal of up to 15 $^{40}\mathrm{Ca}^+$ ions is trapped in a linear Paul trap with trapping frequencies of $\omega_x =$ $2\pi \times 2.924$ MHz (radially) and $\omega_{\rm ax} = 2\pi \times 0.217$ MHz (axially). The qubit states $|z+\rangle$ and $|z-\rangle$ are coupled by an optical quadrupole transition, which we drive with a titanium-sapphire laser, with a sub-10 Hz linewidth, at 729 nm. Collective qubit operations are implemented with a resonant beam that couples to all the qubits with approximately equal strengths. Single-qubit operations are performed with a steerable, tightly focused beam that induces AC Stark shifts. The initial product state (4) is prepared with a fidelity $|\langle \psi_{\rm exp} | \psi_{\rm th} \rangle|^2 = 0.959(4)$. In each experimental cycle, we cool the ions via Doppler cooling and polarisation-gradient cooling [66]. We also sidebandcool all transverse collective motional modes to near their ground states. Then, we prepare the state (4), simulate the Heisenberg evolution, and measure the state. The cycle is repeated 300–500 times per quantum-statetomography measurement basis.

Implementing the effective Heisenberg interaction

We implement the long-range spin-spin interaction (2) with a laser beam carrying two frequencies that couple motional and electronic degrees of freedom of the ion chain. The beam's frequency components, $\omega_{\pm}=\pm(\omega_x+\Delta)$, are symmetrically detuned by $\Delta=2\pi\times25$ kHz (for N=12 ions) from the transverse–center-of-mass mode, which has a frequency $\omega_x=2\pi\times2.924$ MHz. A third frequency component, $\omega_{\rm AC}=2\pi\times1.4$ MHz, is added to the bichromat beam. This component compensates for the additional AC-Stark shift caused by other electronic states [67].

The resulting spin-spin coupling takes the form of a long-range Ising model, $\sum_{j < k} J_{j,k} \sigma_x^{(j)} \sigma_x^{(k)}$. $J_{j,k}$ denotes the strength of the coupling between ions j and k. It approximates the power law in Eq. (2), where the coupling strength equals $J_0 = 606$ rad/s and the exponent $\alpha = 1.02$. The measurements for N = 6, 9 and 15 ions were taken at different axial trapping frequencies $\omega_{\rm ax}$ and different sideband detunings Δ , to keep the power-law exponent approximately constant. The parameters were, for 6 ions, $\omega_{\rm ax} = 2\pi \times 314.8$ kHz, $\Delta = 2\pi \times 29.5$ kHz, $J_0 = 604$ rad/s, $\alpha = 1.02$; for 9 ions, $\omega_{\rm ax} = 2\pi \times 254.9$ kHz, $\Delta = 2\pi \times 26$ kHz, $J_0 = 584$ rad/s, $\alpha = 1.02$; and, for 15 ions, $\omega_{\rm ax} = 2\pi \times 194.1$ kHz, $\Delta = 2\pi \times 23$ kHz, $J_0 = 564$ rad/s, $\alpha = 1.04$.

The desired long-range Heisenberg Hamiltonian (3) cannot easily be realised directly for trapped ions [59, 68]. Instead, we simulate $H_{\rm Heis}$ via Trotterisation. After the first time step, we change the interaction from H_{xx} to H_{yy} ; after the second, to H_{zz} ; and, after the third, back to H_{xx} . We perform this cycle, or Trotter step, $N_{\rm T}$ times [69]. We can realise H_{yy} by shifting the bichromat light's phase by $\pi/2$ relative to the phase used to realise H_{xx} . Implementing H_{zz} requires a global rotation: Denote by R_y a $\pi/2$ rotation of all the qubits about the y-axis. We can effect H_{zz} with, e.g., $R_y^{\dagger}H_{xx}R_y$.

Noise-robust Trotter sequence

In our experimental setup, most decoherence is dephasing relative to the σ_z eigenbasis. This noise results from temporal fluctuations of (i) the magnetic field and (ii) the frequency of the laser that drives the qubits. Earlier experiments on this platform involved XY-interactions, which enable the quantum state to stay in a decoherence-free subspace [5, 67, 70]. Here, the dynamics must be shielded from dephasing differently. We mitigate magnetic-field noise by incorporating a dynamical-decoupling scheme into the Trotter sequence (Fig. 1b). Furthermore, we design the Trotter sequence to minimise the number of global rotations. This minimisation suppresses the error accumulated across all the rotations. We reduce this error further by alternating the rotations' directions between Trotter steps. For further details, see App. E.

To formalise the Trotter sequence, we introduce notation: Let $U_{xx} = \exp(-iH_{xx}t)$ and $U_{yy} = \exp(-iH_{yy}t)$. For $\gamma \in \{x,y\}$, $R_{\gamma} := \exp\left(-i\frac{\pi}{4}\sigma_{\gamma}^{\text{tot}}\right)$ denotes a global $\pi/2$ rotation about the γ -axis. N_{T} denotes the number of Trotter steps. Each Trotter step consists either of the operation $E_+ = U_{yy}U_{xx}R_xU_{yy}$ or the operation $E_- = U_{yy}U_{xx}R_x^{\dagger}U_{yy}$. To simulate a Heisenberg evolution for a time t, we implement the Trotter sequence

$$U_{\rm Heis}(t) \approx R_y^{\dagger} R_x \left[(E_-)^4 (E_+)^4 \right]^{N_{\rm T}/8} R_x^{\dagger} R_y.$$
 (8)

This sequence protects against decoherence and over– /under-rotation errors caused by global pulses. Numerical simulations supporting this claim are presented in App. F.

The Trotter sequence lasts for 15 ms, containing \leq 36 Trotter steps. Each Trotter step consists of three substeps, each lasting for approximately 139 μ s. Each substep's rising and falling slopes are pulse-shaped to avoid incoherent excitations of vibrational sidebands of the qubit transition. The slopes reduce the effective spin-spin coupling by a factor of 0.84, and the actual interaction time is 115 μ s.

The magnetic-field variations occur predominantly at temporally stable 50-Hz harmonics. We reduce the resulting Zeeman-level shifts via feed-forward to a field-compensation coil [8]. The amplitudes end up below 3 Hz, for all 50-Hz harmonics between 50 Hz and 900 Hz. Consider a simple Ramsey experiment on the qubit transition $4^2S_{1/2}(m=+1/2) \leftrightarrow 4^2D_{5/2}(m=+5/2)$. The corresponding (1/e)-contrast coherence time is 47(6) ms. The global qubit rotations are driven by the elliptically

shaped 729-nm beam, which causes spatially inhomogeneous Rabi frequencies that vary across the ion crystal by 6%.

Quantum state tomography

We measure each qubit pair's state via quantum state tomography. In each measurement basis, 300–500 quantum state measurements are carried out. To reconstruct the state from the measurements, we use maximum-likelihood estimation [71]. We estimate statistical uncertainties by bootstrapping [62].

ACKNOWLEDGMENTS

The authors thank Michael Beverland, Ignacio Cirac, Markus Greiner, Julian Léonard, Mikhail Lukin, Vladan Vuletic, and Peter Zoller for insightful conversations. The project leading to this application has received funding from the European Union's Horizon 2020 research and innovation programme under grant agreement No 817482. Furthermore, we acknowledge support from the Austrian Science Fund through the SFB BevondC (F7110) and funding by the Institut für Quanteninformation GmbH. This research was supported in part by the National Science Foundation under Grant No. NSF PHY-1748958, under Grant No. NSF PHY-1748958, and under an NSF grant for the Institute for Theoretical Atomic, Molecular, and Optical Physics at Harvard University and the Smithsonian Astrophysical Observatory.

Appendix A RATE OF HOPPING DURING THE HEISENBERG EVOLUTION

In this section, we derive an expression for the Heisenberg Hamiltonian's spin exchange rate. For simplicity, we model two qubits governed by the Heisenberg Hamiltonian

$$H = \frac{J_0}{3} \left(\sigma_x^{(1)} \sigma_x^{(2)} + \sigma_y^{(1)} \sigma_y^{(2)} + \sigma_z^{(1)} \sigma_z^{(2)} \right). \tag{A1}$$

We relabel the σ_z eigenstates as $|z+\rangle \equiv |\uparrow\rangle$ and $|z-\rangle \equiv |\downarrow\rangle$. Matrices are expressed relative to the basis formed from products of $|\uparrow\rangle$ and $|\downarrow\rangle$. The Hamiltonian can be expressed as

$$H = \frac{J_0}{3} \begin{pmatrix} 1 & 0 & 0 & 0 \\ 0 & -1 & 2 & 0 \\ 0 & 2 & -1 & 0 \\ 0 & 0 & 0 & 1 \end{pmatrix}; \tag{A2}$$

and a pure two-qubit state, as $|\psi(t)\rangle = c_1(t)|\downarrow\downarrow\rangle + c_2(t)|\uparrow\downarrow\rangle + c_3(t)|\downarrow\uparrow\rangle + c_4(t)|\uparrow\uparrow\rangle$. The coefficients $c_k(t) \in \mathbb{C}$ depend on the time, t, and are normalised as $\sum_{k=1}^4 |c_k(t)|^2 = 1$. The dynamics obey the Schrödinger equation, $H|\psi(t)\rangle = i\hbar \frac{\partial |\psi(t)\rangle}{\partial t}$. Defining $\Omega := \frac{J_0}{3}$ and setting $\hbar = 1$, we express the Schrödinger equation in matrix form as

$$\begin{pmatrix} \dot{c}_1(t) \\ \dot{c}_2(t) \\ \dot{c}_3(t) \\ \dot{c}_4(t) \end{pmatrix} = -i\Omega \begin{pmatrix} 1 & 0 & 0 & 0 \\ 0 & -1 & 2 & 0 \\ 0 & 2 & -1 & 0 \\ 0 & 0 & 0 & 1 \end{pmatrix} \begin{pmatrix} c_1(t) \\ c_2(t) \\ c_3(t) \\ c_4(t) \end{pmatrix}.$$
 (A3)

The solution is

$$\begin{cases}
c_1(t) = c_1(0)e^{-i\Omega t} \\
c_2(t) = \frac{1}{2}c_2(0)e^{-i\Omega t}(1 + e^{4i\Omega t}) + \frac{1}{2}c_3(0)e^{-i\Omega t}(1 - e^{4i\Omega t}) \\
c_3(t) = \frac{1}{2}c_3(0)e^{-i\Omega t}(1 + e^{4i\Omega t}) + \frac{1}{2}c_2(0)e^{-i\Omega t}(1 - e^{4i\Omega t}) \\
c_4(t) = c_4(0)e^{-i\Omega t}
\end{cases}$$
(A4)

We aim to derive the time required for $|\uparrow\downarrow\rangle$ to transform into $|\downarrow\uparrow\rangle$. If the initial state is $|\psi(0)\rangle = |\uparrow\downarrow\rangle$, the solution reduces to

$$\begin{cases} c_1(t) = 0 \\ c_2(t) = \frac{1}{2}e^{-i\Omega t}(1 + e^{4i\Omega t}) \\ c_3(t) = \frac{1}{2}e^{-i\Omega t}(1 - e^{4i\Omega t}) \\ c_4(t) = 0 \end{cases}.$$

Consider measuring the σ_z product eigenbasis at time t. The possible outcomes $\uparrow \downarrow$ and $\downarrow \uparrow$ result with probabilities

$$|c_2(t)|^2 = \frac{1}{4}(2 + e^{4i\Omega t} + e^{-4i\Omega t}) = \frac{1}{2} + \frac{1}{2}\cos(4\Omega t)$$
 and (A5)

$$|c_3(t)|^2 = 1 - |c_2(t)|^2$$
. (A6)

Therefore, the two-qubit excitation-hopping frequency is $\Gamma_{\text{flip-flop}} = 4\Omega = 4J_0/3$. The corresponding period is defined as the hopping time:

$$T_{\text{hop}} = \frac{2\pi}{2\Gamma_{\text{flip-flop}}} = \frac{3\pi}{4J_0}.$$
 (A7)

This result agrees with our experimental results and can be extended simply to N qubits. If the interaction is nearest-neighbour only, the time for hopping from site 1 to site N is $T_{\text{hop}} = (N-1)\frac{3\pi}{4L}$.

Appendix B INITIAL STATE

If the global system is prepared in $|\psi_0\rangle$ [Eq. (4)], ρ_{NATS} models a small system's long-time state distinctly more accurately than other thermal states (ρ_{can} and ρ_{GC}) do, at all the global system sizes N realised (Fig. 3). Equation (4) distinguishes ρ_{NATS} for two reasons.

First, suppose that the temperature is high $(\beta \gtrsim 0)$. All the thermal states resemble the maximally mixed (infinite-temperature) state $\mathbbm{1}^{\otimes N}/2^N$ and so resemble each other. We therefore keep the temperature low, by keeping each charge's spatial density low: We separate the $|\gamma+\rangle$'s from each other maximally, for each $\gamma=x,y,z$. To provide a sense of β 's size at N=12, we compare with the bandwidth of the Heisenberg Hamiltonian (3), the greatest energy minus the least. β equals -1.78 times the bandwidth's inverse and -4.24×10^{-4} times the average energy gap's inverse.

Second, noncommuting charges distinguish NATS thermodynamics from more-classical thermodynamics. If we are to observe NATS physics, therefore, ρ_{NATS} [Eq. (1)] should depend significantly on Q_{γ}^{tot} , for all γ . Hence the μ_{γ} 's should have large magnitudes—and so should the expectation values $\langle \psi_0 | \sigma_{\gamma}^{\text{tot}} | \psi_0 \rangle$, by Eq. (6). Hence, for each γ , the σ_{γ} eigenstates in $|\psi_0\rangle$ should be identical. The ordering of the x+,y+, and z+ in Eq. (4) does not matter. Importantly, $|\psi_0\rangle$ is not an eigenstate of any Q_{γ}^{tot} ; so the global system does not begin in a microcanonical subspace; so the experiment is not equivalent, by any global rotation, to any experiment that conserves just σ_z^{tot} and that leads to ρ_{GC} . When N=12, $\beta\mu_z$ equals -0.145 times the inverse of each nonzero gap of S_z^{tot} .

We numerically identified many tensor products of $|\gamma\pm\rangle$'s, as well as superpositions of energy eigenstates, that have β 's much greater than our β . These states suffer from drawbacks that render the states unsuitable for observing the NATS: Either $\mu_{x,y,z}=0$ or only one of the three charges has a nonzero expectation value. Such states reveal nothing about noncommutating charges. Furthermore, the states are highly entangled and so are difficult to prepare experimentally. $|\psi_0\rangle$ is easy to generate, aside from having a large $\sum_{\gamma} \beta \mu_{\gamma} S_{\gamma}^{\rm tot}$.

Appendix C DISTINCTION BETWEEN NON-ABELIAN THERMAL STATE AND COMPETITORS AT ALL GLOBAL SYSTEM SIZES

The main text answers a question established in [22]: Consider a global system of N subsystems, which exchange noncommuting charges. Consider measuring one subsystem's long-time state. Measure the state's distance to ρ_{NATS}

and to the competitor thermal states: the canonical ρ_{can} and the grand canonical ρ_{GC} . The NATS was found, in [22], to predict the final state most accurately. However, as N grew, ρ_{can} and ρ_{GC} approached ρ_{NATS} in accuracy. The reason was believed to be the initial global state, which had a high temperature and low chemical potentials (see Methods). Does ρ_{NATS} remain substantially more accurate at all N, for any initial state $|\psi_0\rangle$? Or do all the thermal states' predictions converge in the thermodynamic limit (as $N \to \infty$), for every $|\psi_0\rangle$?

Our experiment suggests the former, as explained in this paper's Results. We constructed a $|\psi_0\rangle$ for which the NATS prediction remains more accurate than the $\rho_{\rm can}$ and $\rho_{\rm GC}$ predictions, by approximately constant-in-N amounts, at all N values realised experimentally. (Fig. 3). The Methods provides one perspective on why this $|\psi_0\rangle$ distinguishes the thermal states. We provide another perspective here.

We prove that, under conditions realised in our experiment, ρ_{NATS} , averaged over space, differs from the average ρ_{can} and ρ_{GC} . This difference remains nonzero even in the thermodynamic limit. App. C 1 presents the setup, which is more general than our experiment's. In App. C 2, we formalise and prove the result. App. C 3 shows how our experiment realises the general setup.

C 1 Setup

Consider a global system of N identical subsystems. Let $O^{(j)}$ denote observable O of subsystem j. Sometimes, $O^{(j)}$ will implicitly be padded with identity operators $\mathbbm{1}$ acting on the other subsystems. The corresponding global observable is $O^{\text{tot}} := \sum_{j=1}^{N} O^{(j)}$.

The Hamiltonian H^{tot} is translationally invariant. H^{tot} conserves global charges $Q_{\gamma}^{\text{tot}} := \sum_{j=1}^{N} Q_{\gamma}^{(j)}$, for $\gamma = 0, 1, 2, \ldots, c$. The charges do not all commute pairwise: $[Q_{\gamma}^{(j)}, Q_{\gamma'}^{(j)}] \neq 0$ for at least one pair (γ, γ') .

We assume that some global unitary V satisfies two requirements. First, the unitary commutes with the Hamiltonian: $[V, H^{\text{tot}}] = 0$. Second, conjugating at least one global charge Q_{γ}^{tot} with U negates the charge:

$$VQ_{\gamma}^{\text{tot}}V^{\dagger} = -Q_{\gamma}^{\text{tot}}.$$
 (C1)

We assume that this global charge's initial expectation value is proportional to the global system size, as in the trapped-ion experiment:

$$\left\langle Q_{\gamma}^{\mathrm{tot}}\right\rangle _{0}=q_{\gamma}N\neq0,$$
 (C2)

for some constant-in- $N q_{\gamma}$.

Let $|\psi_0\rangle$ denote the initial global state. It is invariant, we assume, under translations through τ sites, for some nonnegative integer τ . More precisely, divide the chain into clumps of τ subsystems. Index the clumps with $m=1,2,\ldots,N/\tau$. (We assume for convenience that N is an integer multiple of τ .) Consider tracing out all the subsystems except the m^{th} clump: $\text{Tr}_{1,2,\ldots,(m-1)\tau,\ m\tau+1,m\tau+2,\ldots,N}(|\psi_0\rangle\langle\psi_0|)$. This state's form does not depend on m.

Let us define a state averaged over clumps of subsystems. Let ρ denote any state of the global system. Consider the clump that, starting at subsystem j, encompasses τ subsystems. This clump occupies the state

$$\rho^{(j,j+1,\dots,j+\tau-1)} := \operatorname{Tr}_{1,2,\dots,j-1,\ j+\tau,j+\tau+1,\dots,N}(\rho). \tag{C3}$$

Let \mathcal{T}_j denote the operator that translates a state j-1 sites leftward. We define the average

$$\rho^{\text{avg}} := \frac{1}{N} \sum_{j=1}^{N} \mathcal{T}_j \left(\rho^{(j,j \oplus 1, \dots, j \oplus \tau \ominus 1)} \right)$$
 (C4)

on the joint Hilbert space of subsystems 1 through τ . Addition and subtraction modulo N are denoted by \oplus and \ominus . If ρ is fully translationally invariant (if $\tau=1$), then $\rho^{\text{avg}}=\text{Tr}_{2,3,\ldots,N}(\rho)$, and this definitional step can be skipped.

Multiple thermal states will interest us. The global canonical state is defined as $\rho_{\text{can}}^{\text{tot}} := \exp(-\beta H^{\text{tot}})/Z_{\text{can}}^{\text{tot}}$. The partition function is $Z_{\text{can}}^{\text{tot}} := \text{Tr}(e^{-\beta H^{\text{tot}}})$. The inverse temperature β is defined through $\langle \psi_0 | H^{\text{tot}} | \psi_0 \rangle = \text{Tr}(H^{\text{tot}} \rho_{\text{can}}^{\text{tot}})$. Define the single-site $\rho_{\text{can}}^{(j)} := \text{Tr}_{\bar{j}}(\rho_{\text{can}}^{\text{tot}})$. Denote by $\rho_{\text{can}}^{\text{avg}}$ the result of averaging $\rho_{\text{can}}^{\text{tot}}$ over clumps, as in Eq. (C4).

¹ We thank Ignacio Cirac for framing this argument.

The global NATS is defined as

$$\rho_{\text{NATS}}^{\text{tot}} := \exp\left(-\beta \left[H^{\text{tot}} - \sum_{\gamma=1}^{c} \mu_{\gamma} Q_{\gamma}^{\text{tot}}\right]\right) / Z_{\text{NATS}}^{\text{tot}}.$$
 (C5)

This β is defined analogously to the canonical β . The temperatures' values might differ, but we reuse the symbol β for convenience. The effective chemical potentials μ_{γ} are defined through [22]

$$q_{\gamma}N = \text{Tr}\left(Q_{\gamma}^{\text{tot}}\rho_{\text{NATS}}^{\text{tot}}\right). \tag{C6}$$

The partition function $Z_{\mathrm{NATS}}^{\mathrm{tot}} := \mathrm{Tr} \left(e^{-\beta \left(H^{\mathrm{tot}} - \sum_{\gamma=1}^{c} \mu_{\gamma} Q_{\gamma}^{\mathrm{tot}} \right)} \right)$. Define $\rho_{\mathrm{NATS}}^{(j)}$ and $\rho_{\mathrm{NATS}}^{\mathrm{avg}}$ analogously to $\rho_{\mathrm{can}}^{(j)}$ and $\rho_{\mathrm{can}}^{\mathrm{avg}}$. Our argument concerns multiple distance measures. Let O denote an arbitrary observable defined on an arbitrary Hilbert space. The Schatten p-norm of O is $||O||_p := [\mathrm{Tr} \left(|O|^p \right)]^{1/p}$, wherein $|O| := \sqrt{O^{\dagger}O}$ and $p \in [0, \infty)$. The limit as $p \to \infty$ yields the operator norm: $\lim_{p \to \infty} ||O||_p := ||O||_{\mathrm{op}}$. Let ρ and σ denote operators defined on an arbitrary Hilbert space. The Schatten p-distance between the states is $||\rho - \sigma||_p$. The trace distance is $\mathcal{D}_{\mathrm{tr}}(\rho, \sigma) = \frac{1}{2} ||\rho - \sigma||_1$.

C 2 Lower bounds on distances between thermal states

We now formalise the result.

Theorem 1. Let the setup and definitions be as in the previous subsection. Consider the distance from the average NATS to the average canonical state. Measured with the Schatten 1-distance or the relative entropy, this distance obeys the lower bound

$$D\left(\rho_{\text{NATS}}^{\text{avg}}||\rho_{\text{can}}^{\text{avg}}\right) \ge \mathcal{D}_{\text{tr}}\left(\rho_{\text{NATS}}^{\text{avg}}, \rho_{\text{can}}^{\text{avg}}\right) \ge \frac{|q_{\gamma}|}{\left\|Q_{\gamma}^{(j)}\right\|_{\text{op}}} > 0,$$
(C7)

for an arbitrary j = 1, 2, ..., N. ρ_{can} can be replaced with any grand canonical state that commutes with V.

The bound does not depend on N and so holds in the thermodynamic limit.

Proof. The proof has the following outline. First, we calculate the expectation value of $Q_{\gamma}^{(1)}$ in $\rho_{\text{NATS}}^{\text{avg}}$; the result is q_{γ} . Second, the expectation value in $\rho_{\text{can}}^{\text{avg}}$ vanishes, we show using V. Because the two expectation values differ, a nonzero Schatten 1-distance separates the states. The Schatten 1-distance lower-bounds the relative entropy via Pinsker's inequality.

 $Q_{\gamma}^{(1)}$ has an expectation value, in the average NATS state, of

$$\operatorname{Tr}(Q_{\gamma}^{(1)}\rho_{\text{NATS}}^{\text{avg}}) = \frac{1}{N} \sum_{j=1}^{N} \operatorname{Tr}\left(Q_{\gamma}^{(1)} \mathcal{T}_{j}\left(\rho_{\text{NATS}}^{(j,j\oplus 1,\dots,j\oplus \tau\ominus 1)}\right)\right)$$
(C8)

$$= \frac{1}{N} \sum_{j=1}^{N} \operatorname{Tr} \left(Q_{\gamma}^{(j)} \rho_{\text{NATS}}^{(j)} \right) \tag{C9}$$

$$= \frac{1}{N} \operatorname{Tr} \left(\left[\sum_{j=1}^{N} \mathbb{1}^{\otimes (j-1)} \otimes Q_{\gamma}^{(j)} \otimes \mathbb{1}^{\otimes (N-j)} \right] \left[\bigotimes_{k=1}^{N} \rho_{\text{NATS}}^{(k)} \right] \right)$$
 (C10)

$$= \frac{1}{N} \text{Tr} \left(Q_{\gamma}^{\text{tot}} \rho_{\text{NATS}}^{\text{tot}} \right) \tag{C11}$$

$$=q_{\gamma}.\tag{C12}$$

Equation (C9) follows from the definition of \mathcal{T}_{j} . Equation (C12) follows Eq. (C6).

The analogous canonical expectation value vanishes, we show next. We begin with the global expectation value $\text{Tr}(Q_{\gamma}^{\text{tot}}\,e^{-\beta H^{\text{tot}}})/Z_{\text{can}}^{\text{tot}}$. By Eq. (C1), we can replace the Q_{γ}^{tot} with $-VQ_{\gamma}^{\text{tot}}V^{\dagger}$. We then invoke the trace's cyclicality:

$$\operatorname{Tr}\left(Q_{\gamma}^{\operatorname{tot}}e^{-\beta H^{\operatorname{tot}}}\right)/Z_{\operatorname{can}}^{\operatorname{tot}} = -\operatorname{Tr}\left(\left[VQ_{\gamma}^{\operatorname{tot}}V^{\dagger}\right]e^{-\beta H^{\operatorname{tot}}}\right)/Z_{\operatorname{can}}^{\operatorname{tot}} = -\operatorname{Tr}\left(Q_{\gamma}^{\operatorname{tot}}\left[V^{\dagger}e^{-\beta H^{\operatorname{tot}}}V\right]\right)/Z_{\operatorname{can}}^{\operatorname{tot}}$$
(C13)

$$= -\text{Tr}\left(Q_{\gamma}^{\text{tot}}e^{-\beta H^{\text{tot}}}\right)/Z_{\text{can}}^{\text{tot}}.$$
(C14)

Equation (C14) follows from $[V, H^{\text{tot}}] = 0$. Let us compare the beginning and end of Eqs. (C13)–(C14). The expectation value $\operatorname{Tr}\left(Q_{\gamma}^{\operatorname{tot}}\,e^{-\beta H^{\operatorname{tot}}}\right)/Z_{\operatorname{can}}^{\operatorname{tot}}$ equals its negative and so vanishes. We can re-express the null expectation value in terms of the average canonical state:

$$0 = \sum_{j=1}^{N} \operatorname{Tr} \left(Q_{\gamma}^{\text{tot}} e^{-\beta H^{\text{tot}}} \right) / Z_{\text{can}}^{\text{tot}}$$
(C15)

$$= \sum_{j=1}^{N} \operatorname{Tr} \left(\left[\mathbb{1}^{\otimes (j-1)} \otimes Q_{\gamma}^{(j)} \otimes \mathbb{1}^{\otimes (N-j)} \right] e^{-\beta H^{\text{tot}}} \right) / Z_{\text{can}}^{\text{tot}} = \sum_{j=1}^{N} \operatorname{Tr} \left(Q_{\gamma}^{(j)} \operatorname{Tr}_{\bar{j}} \left(e^{-\beta H^{\text{tot}}} \right) \right) / Z_{\text{can}}^{\text{tot}}$$
(C16)

$$= \sum_{j=1}^{N} \operatorname{Tr}_{j} \left(Q_{\gamma}^{(j)} \rho_{\operatorname{can}}^{(j)} \right) \tag{C17}$$

$$= \sum_{j=1}^{N} \operatorname{Tr} \left(Q_{\gamma}^{(1)} \mathcal{T}_{j} \left(\rho_{\operatorname{can}}^{(j,j\oplus 1,\dots,j\oplus \tau\ominus 1)} \right) \right) \tag{C18}$$

$$= \operatorname{Tr}\left(Q_{\gamma}^{(1)}\rho_{\operatorname{can}}^{\operatorname{avg}}\right). \tag{C19}$$

Equations (C17) and (C18) are analogous to Eqs. (C9) and (C8).

We have calculated two expectation values of Q_{γ}^1 , one in $\rho_{\text{NATS}}^{\text{avg}}$ and one in $\rho_{\text{can}}^{\text{avg}}$. The two expectation values differ, by Eqs. (C15), (C19), and (C12):

$$\left| \operatorname{Tr} \left(Q_{\gamma}^{(1)} \rho_{\text{NATS}}^{\text{avg}} \right) - \operatorname{Tr} \left(Q_{\gamma}^{(1)} \rho_{\text{can}}^{\text{avg}} \right) \right| = |q_{\gamma}| > 0.$$
 (C20)

The absolute difference (C20), we can relate to the trace distance. Let ρ and σ denote quantum states defined on an arbitrary Hilbert space. The interstate distance equals a supremum over observables O defined on the same space [72, Lemma 9.1.1]:

$$\mathcal{D}_{tr}(\rho, \sigma) = \sup_{O: ||O||_{op} \le 1} \left\{ |\operatorname{Tr}(\rho O) - \operatorname{Tr}(\sigma O)| \right\}. \tag{C21}$$

Let $\rho = \rho_{\mathrm{NATS}}^{\mathrm{avg}}$ and $\sigma = \rho_{\mathrm{can}}^{\mathrm{avg}}$. The operator $Q_{\gamma}^{(1)}/||Q_{\gamma}^{(1)}||_{\mathrm{op}}$ is one normalized O. Therefore, by Eq. (C20), $\frac{|q_{\gamma}|}{||Q_{\gamma}^{(1)}||_{\mathrm{op}}}$ lower-bounds the supremum in (C21). The superscript (1) can be replaced with (j), due to translation invariance in the \mathcal{T}_j argument. Hence $\mathcal{D}_{\text{tr}}(\rho_{\text{NATS}}^{\text{avg}}, \rho_{\text{can}}^{\text{avg}}) \geq \frac{|q_{\gamma}|}{||Q_{\gamma}^{(j)}||_{\text{lop}}} > 0$. The final inequality follows from (i) the assumption (C2) and (ii) the finiteness of the single-subsystem $||Q_{\gamma}^{(j)}||_{\text{op}}$. The first inequality in (C7) follows via Pinsker's inequality: For states ρ and σ , $D(\rho||\sigma) \geq \mathcal{D}_{tr}(\rho,\sigma)$. This proof remains true if ρ_{GC} replaces ρ_{can} and $[\rho_{GC}, V] = 0$.

C 3 Realisation in trapped-ion experiment

The general setup of App. C 1 can be realised in the main text's trapped-ion experiment. In the simplest realisation, $Q_{\gamma} = \sigma_x$. The unitary $V = \sigma_z^{\otimes 2N}$:

$$V\sigma_x^{\text{tot}}V^{\dagger} = \sigma_z^{\otimes 2N} \left(\sum_{j=1}^N \sigma_x^{(j)}\right) \sigma_z^{\otimes 2N} = \sum_{j=1}^N \left(-\sigma_x^{(j)}\right) = -\sigma_x^{\text{tot}}.$$
 (C22)

The initial state is $|\psi_0\rangle = |x+,y+,z+\rangle^{\otimes 2N/3}$, so $\langle \psi_0|\sigma_x^{\rm tot}|\psi_0\rangle \propto N$, and the state is invariant under translations through $\tau=3$ sites. Define $\rho_{\rm GC}^{\rm tot}:=\exp\left(-\beta\left[H^{\rm tot}-\mu_zS_z^{\rm tot}\right]\right)/Z_{\rm GC}^{\rm tot}$. The effective chemical potential μ_z is defined as in the main text, and $Z_{\rm GC}^{\rm tot}$ normalises the state. $\rho_{\rm GC}^{\rm tot}$ can replace the canonical state in Ineq. (C7). The mapping just described is conceptually simple. However, we find analytically, another mapping achieves the tightest bound (C7): $\frac{1}{\sqrt{3}}\left(\sigma_x+\sigma_y+\sigma_z\right)$, and $V=\left[\frac{1}{\sqrt{6}}(2\sigma_x-\sigma_y-\sigma_z)\right]^{\otimes N}$. (Alternatively, the σ_γ 's in V can be permuted in any way.)

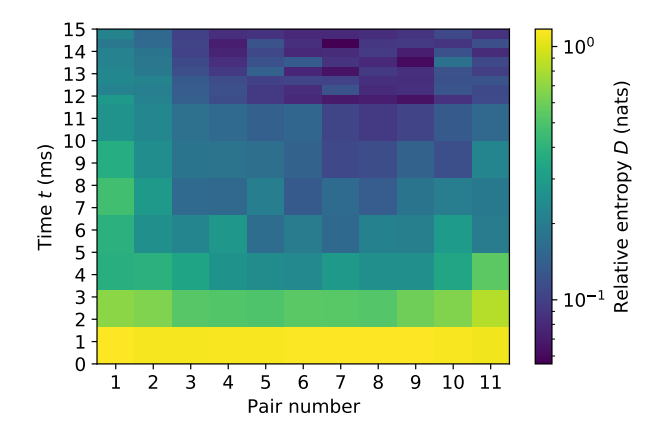


FIG. 4: Relative entropy to the NATS for each qubit pair, as a function of time: The spatio-temporal fluctuations show that different qubit pairs thermalise to different extents. The chain consists of N = 12 ions.

Appendix D SPATIO-TEMPORAL FLUCTUATIONS IN STATES' DISTANCES TO THE NON-ABELIAN THERMAL STATE

Figure 4 shows the experimentally observed fluctuations, across space and time, of the relative entropy to the NATS. The chain consists of N = 12 ions. Every ion pair's state approaches the NATS in time. However, nonuniformity remains; edge pairs thermalise more slowly due to edge effects, while the central pairs thermalise more quickly.

Appendix E DERIVATIONS OF TROTTER SEQUENCES

The evolution implemented differs from evolution under the Heisenberg Hamiltonian (3) for three reasons. First, the Heisenberg Hamiltonian is Trotter-approximated. Second, parts of the Trotter approximation are simulated via native interactions dressed with rotations. Third, we reduce decoherence via dynamical decoupling. Here, we derive the experimental pulse sequence. We review parts of the setup and introduce notation in App. E 1. In App. E 2, we detail the two errors against which the pulse sequence protects. We derive the pulse sequence in App. E 3. App. E 4 extends the derivation from the Heisenberg evolution to the XY model (7).

E 1 Quick review of setup and notation

We break a length-t time interval into $N_{\rm T}$ steps of length $t/N_{\rm T} =: \Delta t$ each. We aim to simulate the Heisenberg Hamiltonian (3), whose $J_0/|j-k|^{\alpha}$ we sometimes denote by $J_{j,k}$ here. $H_{\rm Heis}$ generates the family of unitaries $U_{\rm Heis}(t) := e^{-iH_{\rm Heis}t}$. To effect this family, we leverage single-axis Hamiltonians

$$H_{\gamma\gamma} := \sum_{j=1}^{N} \sum_{k>j} J_{j,k} \, \sigma_{\gamma}^{(j)} \sigma_{\gamma}^{(k)}. \tag{E1}$$

 H_{xx} and H_{yy} are native to the experimental platform. The Hamiltonians (E1) generate the unitaries $e^{-iH_{\gamma\gamma}\Delta t} =: U_{\gamma\gamma}$. We interleave the interaction with rotations $R_{\gamma} := \exp\left(-i\frac{\pi}{4}\sigma_{\gamma}^{\text{tot}}\right)$, for $\gamma = x, y, z$. We denote the single-qubit identity operator by $\mathbb{1}$.

E 2 Two sources of error

Our pulse sequence combats detuning and rotation errors. The detuning error manifests as an undesired term that creeps into the Hamiltonian (3). Proportional to $\sigma_z^{\rm tot}$, the term represents an external magnetic field. We protect against the detuning error with dynamical decoupling: The detuning error undesirably rotates each ion's state about

the z-axis. We apply a π -pulse about the x-axis, reflecting the state through the xy-plane. The state then precesses about the z-axis oppositely, undoing the earlier precession. Another π -pulse undoes the reflection.

The second error plagues the engineered rotations: A qubit may rotate too little or too much, because the ion string is illuminated not quite uniformly. We therefore replace certain rotations R_{γ} with R_{γ}^{\dagger} 's. An ion may rotate too much while undergoing R_{γ} but, while undergoing R_{γ}^{\dagger} , rotates through the same angle oppositely. The excess rotations cancel.

E 3 Derivation of Trotter sequence

First, we divvy up the Heisenberg evolution into steps. Then, we introduce rotations that enable dynamical decoupling. We Trotter-approximate a Heisenberg step in two ways. Alternating the two Trotter approximations across a pulse sequence mitigates rotation errors.

To simulate the Heisenberg Hamiltonian for a time t, we evolve for $N_{\rm T}$ length- Δt time steps: $U_{\rm Heis}(t) = [U_{\rm Heis}(\Delta t)]^{N_{\rm T}}$. To facilitate dynamical decoupling, we insert an identity operator on the left: $U_{\rm Heis}(t) = \mathbbm{1}^{\otimes N} [U_{\rm Heis}(\Delta t)]^{N_{\rm T}}$. We decompose the $\mathbbm{1}^{\otimes N}$ into rotations about the z-axis. How this decomposition facilitates dynamical decoupling is not yet obvious, as the rotations commute with the detuning expression. Later, though, we will commute some of the rotations across interaction unitaries. The commutation will transform the z-rotations into R_x 's. For now, we decompose the $\mathbbm{1}^{\otimes N}$ in two ways:

$$U_{\text{Heis}}(t) = (R_z^{\dagger})^{N_{\text{T}}} (R_z)^{N_{\text{T}}} [U_{\text{Heis}}(\Delta t)]^{N_{\text{T}}}$$
 (E2)

$$= (R_z)^{N_{\rm T}} (R_z^{\dagger})^{N_{\rm T}} [U_{\rm Heis}(\Delta t)]^{N_{\rm T}} . \tag{E3}$$

We will implement the right-hand side of (E2) during half the protocol and, during the other half, implement (E3). This alternation will mitigate rotation errors.

Let us analyze (E2), then (E3). R_z commutes with $U_{\text{Heis}}(\Delta t)$ because the Heisenberg Hamiltonian conserves σ_z^{tot} : $[H_{\text{Heis}}, \sigma_z^{\text{tot}}] = 0$ implies that $[U_{\text{Heis}}(\Delta t), R_z] = 0$. The R_z 's of Eq. (E2) can therefore move inside the square brackets:

$$U_{\text{Heis}}(t) = (R_z^{\dagger})^{N_{\text{T}}} \left[R_z U_{\text{Heis}}(\Delta t) \right]^{N_{\text{T}}} . \tag{E4}$$

We Trotter-approximate the short Heisenberg evolution as

$$U_{\text{Heis}}(\Delta t) \approx U_{yy}U_{zz}U_{xx}.$$
 (E5)

The ordering of the directions is arbitrary.

We substitute into (E4) and rewrite the bracketed factor, pursuing three goals. First, the U_{zz} is not native to our platform. We therefore simulate it with $R_y^{\dagger}U_{xx}R_y$. Second, one R_x must end up amidst the $U_{\gamma\gamma}$'s. Two blocks of $U_{\gamma\gamma}$'s, each containing an R_x , will consequently effect one π pulse. Composing these π pulses will effect dynamical decoupling. Third, any other, stray R_{γ} 's must be arranged symmetrically on either side of the $U_{\gamma\gamma}$'s, as explained below.

Let us replace the U_{zz} in (E5) with $R_y^{\dagger}U_{xx}R_y$.² The R_y^{\dagger} commutes across the U_{yy} :

$$R_z U_{yy} U_{zz} U_{xx} = R_z U_{yy} (R_y^{\dagger} U_{xx} R_y) U_{xx} = R_z R_y^{\dagger} U_{yy} U_{xx} R_y U_{xx}. \tag{E6}$$

We have eliminated the U_{zz} . Similarly eliminating the R_z will prove useful, so we invoke $R_z = R_v^{\dagger} R_x R_y$:

$$R_z U_{yy} U_{zz} U_{xx} = (R_y^{\dagger} R_x R_y) R_y^{\dagger} U_{yy} U_{xx} R_y U_{xx} = (R_y^{\dagger} R_x) U_{yy} U_{xx} R_y U_{xx}. \tag{E7}$$

We will benefit from complementing the $R_y^{\dagger}R_x$ with a mirror image $(R_y^{\dagger}R_x)^{\dagger} = R_x^{\dagger}R_y$ on the right: We will implement $R_zU_{yy}U_{zz}U_{xx}$ many times, and instances of the left-hand $R_y^{\dagger}R_x$ will cancel instances of the right-hand $R_x^{\dagger}R_y$. Therefore, we insert $\mathbb{1}^{\otimes N} = R_y^{\dagger}R_xR_x^{\dagger}R_y$ into the right-hand side of (E7):

$$R_z U_{yy} U_{zz} U_{xx} = (R_y^{\dagger} R_x) U_{yy} U_{xx} \underbrace{R_y U_{xx} (R_y^{\dagger} R_x R_x^{\dagger} R_y)}_{=U_{xx}}. \tag{E8}$$

 $\cos(\pi/4)\mathbbm{1}^{\otimes N} - i\sin(\pi/4)\sigma_y^{\mathrm{tot}}$, multiplying out, and invoking $\sigma_\lambda\sigma_\nu = i\varepsilon_{\lambda\nu\xi}\sigma_\xi$. The result is the Taylor series for U_{zz} .

² One can prove the expressions' equality by writing out the Taylor series for $U_{xx} = \exp(i\Delta t H_{xx})$, conjugating each term with the rotations, invoking the Euler decomposition $R_y =$

Again, U_{zz} is not native to our platform. We therefore commute the R_x across the U_{zz} , invoking $R_x^{\dagger}U_{zz}R_x = U_{yy}$:

$$R_z U_{yy} U_{zz} U_{xx} = (R_y^{\dagger} R_x) \underbrace{U_{yy} U_{xx} R_x U_{yy}}_{=:E_+} (R_x^{\dagger} R_y). \tag{E9}$$

The final expression has the sought-after form. We substitute into Eq. (E5), then into Eq. (E4), and then cancel rotations: $U_{\text{Heis}}(t) \approx (R_z^{\dagger})^{N_{\text{T}}} (R_y^{\dagger} R_x) (E_+)^{N_{\text{T}}} (R_x^{\dagger} R_y).$

Suppose that $N_T = 4$. The E_+ 's, containing four R_x 's total, implement two π pulses—one round of dynamical decoupling. Furthermore, $(R_z^{\dagger})^4 = (-1)^{N_T} \mathbb{1}^{\otimes N}$, so

$$U_{\text{Heis}}(4\Delta t) \approx (R_z^{\dagger})^4 (R_y^{\dagger} R_x) (E_+)^4 (R_x^{\dagger} R_y) = (-1)^N (R_y^{\dagger} R_x) (E_+)^4 (R_x^{\dagger} R_y). \tag{E10}$$

Now, let $N_{\rm T} \gg 4$, as in the experiment. After one round of dynamical decoupling, to mitigate the detuning error, we mitigate rotation errors. We effect four time steps with an alternative operator derived from Eq. (E3). Then, we continue alternating.

Let us derive the alternative to E_+ . We shift the R_z^{\dagger} 's of Eq. (E3) inside the square brackets:

$$U_{\text{Heis}}(t) = (R_z)^{N_{\text{T}}} \left[R_z^{\dagger} U_{\text{Heis}}(\Delta t) \right]^{N_{\text{T}}} \approx (R_z)^{N_{\text{T}}} \left[R_z^{\dagger} U_{yy} U_{zz} U_{xx} \right]^{N_{\text{T}}} . \tag{E11}$$

The final expression follows from Eq. (E5). The bracketed factor must end up with the $(R_y^{\dagger}R_x)[\ldots](R_x^{\dagger}R_y)$ structure of Eq. (E9), so that rotations cancel between instances of (E9) and instances of the new bracketed factor. We therefore ensure that $R_{\eta}^{\dagger}R_{x}$ is on the factor's left-hand side, then propagate extraneous rotations leftward:

$$\underbrace{R_z^{\dagger}}_{=R_y^{\dagger}R_x^{\dagger}R_y = R_y^{\dagger}\mathbb{1}^{\otimes N}R_x^{\dagger}R_y = R_y^{\dagger}(R_x R_x^{\dagger})R_x^{\dagger}R_y}_{(E12)}$$

$$= R_y^\dagger R_x^\dagger R_y = R_y^\dagger \mathbb{1}^{\otimes N} R_x^\dagger R_y = R_y^\dagger (R_x R_x^\dagger) R_x^\dagger R_y$$

$$= (R_y^{\dagger} R_x)(R_x^{\dagger})^2 \underbrace{R_y U_{yy} U_{zz} U_{xx}}_{=U_{yy} R_y} = (R_y^{\dagger} R_x) R_x^{\dagger} \underbrace{R_x^{\dagger} U_{yy}}_{=U_{zz} R_x^{\dagger}} \underbrace{R_y U_{zz} U_{xx}}_{=U_{xx} R_y}$$
(E13)

$$= (R_y^{\dagger} R_x) \underbrace{R_x^{\dagger} U_{zz}}_{=U_{yy} R_x^{\dagger}} \underbrace{R_x^{\dagger} U_{xx}}_{=U_{xx} R_x^{\dagger}} \underbrace{R_y U_{xx}}_{=U_{zz} R_y} = (R_y^{\dagger} R_x) U_{yy} \underbrace{R_x^{\dagger} U_{xx}}_{=U_{xx} R_x^{\dagger}} \underbrace{R_x^{\dagger} U_{zz}}_{=U_{yy} R_x^{\dagger}} R_y$$
(E14)

$$= (R_y^{\dagger} R_x) \underbrace{U_{yy} U_{xx} R_x^{\dagger} U_{yy}}_{=:E_-} (R_x^{\dagger} R_y). \tag{E15}$$

By Eq. (E11), $U_{\text{Heis}}(t) \approx (R_z)^{N_{\text{T}}} (R_y^{\dagger} R_x) (E_-)^{N_{\text{T}}} (R_x^{\dagger} R_y)$. Analogously to Eq. (E10),

$$U_{\text{Heis}}(4\Delta t) \approx (-1)^N (R_y^{\dagger} R_x) (E_-)^4 (R_x^{\dagger} R_y).$$
 (E16)

We alternate instances of (E10) with instances of (E16) to simulate long Heisenberg evolutions. Many rotations cancel. If $N_{\rm T}$ equals an integer multiple of eight,

$$U_{\text{Heis}}(t) \approx R_y^{\dagger} R_x \left[(E_-)^4 (E_+)^4 \right]^{N_{\text{T}}/8} R_x^{\dagger} R_y.$$
 (E17)

Extension from Heisenberg model to XY model

In the Results, we experimentally compared the Heisenberg evolution with evolution under the XY model, Eq. (7). H_{xy} generates the unitaries $U_{xy}(t) := \exp(-itH_{xy})$. We can more easily Trotterise $U_{xy}(t)$ while mitigating errors than Trotterise $U_{\text{Heis}}(t)$.

As before, we divvy up the evolution into steps. Then, we Trotter-approximate the steps and insert $\mathbb{1}^{\otimes N}$ $\left[\left(R_x^\dagger\right)^2\right]^{N_{\mathrm{T}}}\left(R_x^2\right)^{N_{\mathrm{T}}}:$

$$U_{xy}(t) = [U_{xy}(\Delta t)]^{N_{\rm T}} \approx (U_{yy}U_{xx})^{N_{\rm T}}$$
 (E18)

$$= \left[\left(R_x^{\dagger} \right)^2 \right]^{N_{\rm T}} \left(R_x^2 \right)^{N_{\rm T}} \left(U_{yy} U_{xx} \right)^{N_{\rm T}} . \tag{E19}$$

Due to the square, R_x^2 commutes with $U_{yy}U_{xx}$:

$$R_x^2 U_{yy} U_{xx} = R_x \underbrace{R_x U_{yy}}_{=U_{zz} R_x} U_{xx} = \underbrace{R_x U_{zz}}_{=U_{yy} R_x} R_x U_{xx} = U_{yy} \underbrace{R_x^2 U_{xx}}_{=U_{xx} R_x^2} = U_{yy} U_{xx} R_x^2 . \tag{E20}$$

Therefore, in Eq. (E19), we can pull the $(R_x^2)^{N_T}$ into the parentheses:

$$U_{xy}(t) = \left[\left(R_x^{\dagger} \right)^2 \right]^{N_{\text{T}}} \left(R_x^2 U_{yy} U_{xx} \right)^{N_{\text{T}}}. \tag{E21}$$

We could commute the R_x^2 into the center of the $U_{\gamma\gamma}$'s, to improve the dynamical decoupling. However, Eq. (E21) suffices; errors accumulate in only a couple of gates.

The operator $F_+ := R_x^2 U_{yy} U_{xx}$ contains a π -pulse. Therefore, we need perform F_+ only twice before implementing $F_- := (R_x^{\dagger})^2$. Furthermore, $\left[\left(R_x^{\dagger} \right)^2 \right]^2 = (-1)^N$. If $N_{\rm T}$ is a multiple of four, then $U_{xy}(t) = \left[(F_-)^2 (F_+)^2 \right]^{N_{\rm T}/4}$.

Appendix F ASSESSMENT OF NOISE-ROBUST TROTTER SEQUENCE

App. E describes the Trotter sequence that we engineered to alleviate errors. Here, we demonstrate the sequence's effectiveness in numerical simulations and in the experiment. Figure 5 shows the dynamical decoupling's effects in the parameter regime used experimentally. Constant detuning errors of up to several hundred Hertz do not significantly reduce the time-evolved state's fidelity to the ideal state (< 10% change in fidelity up to 500 Hz detuning error). Similarly, systematic rotation errors of $\pm 10\%$ affect the fidelity little (4% drop in fidelity). If the detunings oscillate temporally, the dynamical decoupling's robustness depends heavily on the oscillation frequency, f: Recall that $t_f = 15$ ms denotes the experiment's temporal length and N_T denotes the number of Trotter steps. Consider an individual qubit state expressed as a combination of outer products of σ_z eigenstates. If f is an integer multiple of $f_1 = \frac{1}{2}(4t_f/N_T)^{-1} = 300$ Hz, the qubit's state acquires a relative phase, reducing the fidelity to the ideal state.

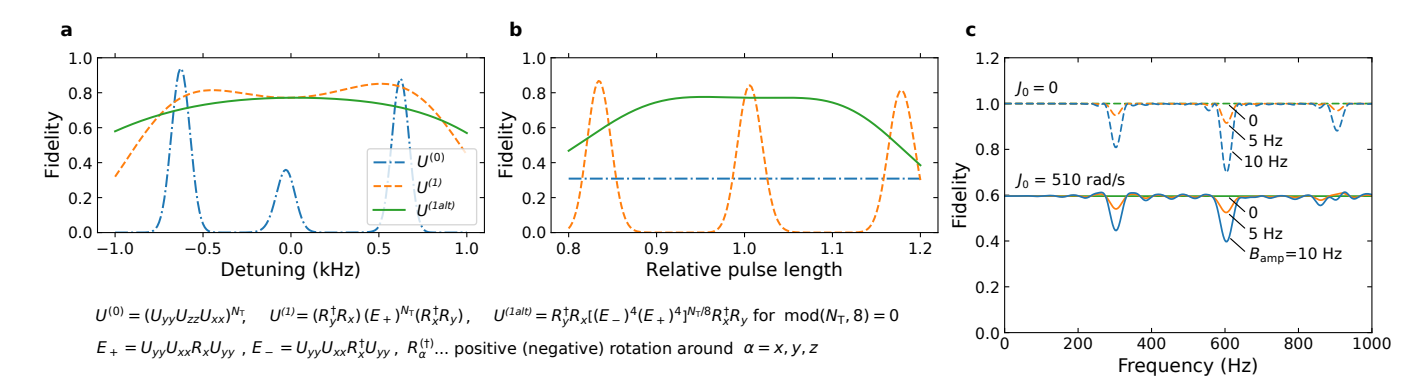


FIG. 5: Dynamical decoupling: The simulation was performed with 12 ions, a power-law approximation to the coupling, $J_0 = 510 \text{ rad/s}$, $\alpha = 1.02$, and 10 ms of evolution. The fidelity compares the simulated Trotter-approximated state with the exact ideal state: $\left(\text{Tr}\sqrt{\sqrt{\rho_{\text{exact}}}\rho_{\text{Trotter}}\sqrt{\rho_{\text{exact}}}}\right)^2$. (a) Introducing $\pi/2$ rotations into the Trotter sequence guards against detuning errors. The right-hand side (RHS) of Eq. (E5) defines the sequence $U^{(0)}$, the RHS of Eq. (E16) defines $U^{(1)}$, and the RHS of Eq. (E17) defines $U^{(1\text{alt})}$. (b) Alternating the rotation's direction guards against systematic rotation errors. (c) Response to oscillations of a time-varying magnetic field $\mathbf{B} = B_{\text{amp}} \cos(2\pi ft)\hat{z}$, wherein $B_{\text{amp}} \geq 0$ (15 ms evolution). The dynamically decoupled Trotter sequence $U^{(1\text{alt})}$ allows the fidelity to drop. The drops occur when the field's frequency, f, is an integer multiple of $f_1 = \frac{1}{2}(4T_{\text{tot}}/N_{\text{Trotter}})^{-1} = 300 \text{ Hz}$. We can understand this behavior most simply when $J_0 = 0$ (top curves): The qubits do not interact, so each qubit remains in a superposition, whose relative phase undesirably changes under \mathbf{B} .

The experimentally observed two-qubit fidelities $\left(\text{Tr}\sqrt{\sqrt{\rho_{\text{exact}}}\rho_{\text{exp}}\sqrt{\rho_{\text{exact}}}}\right)^2$ range from 0.995(4), at t=0, to 0.97(1), at $t=t_{\text{f}}$ (Fig. 6). The fidelity is lower for pairs near the ion crystal's edges than for pairs near the center. This contrast results, at t=0, from imperfections in the state preparation caused by the inhomogeneous profile of the global rotations. At $t=t_{\text{f}}$, the lower fidelities result from global rotation errors in the Trotter sequence: The total number of Trotter steps, 36, is not an integer multiple of 8. Consequently, a period of the alternating Trotter sequence (E17) is not completed, and rotation errors remain.

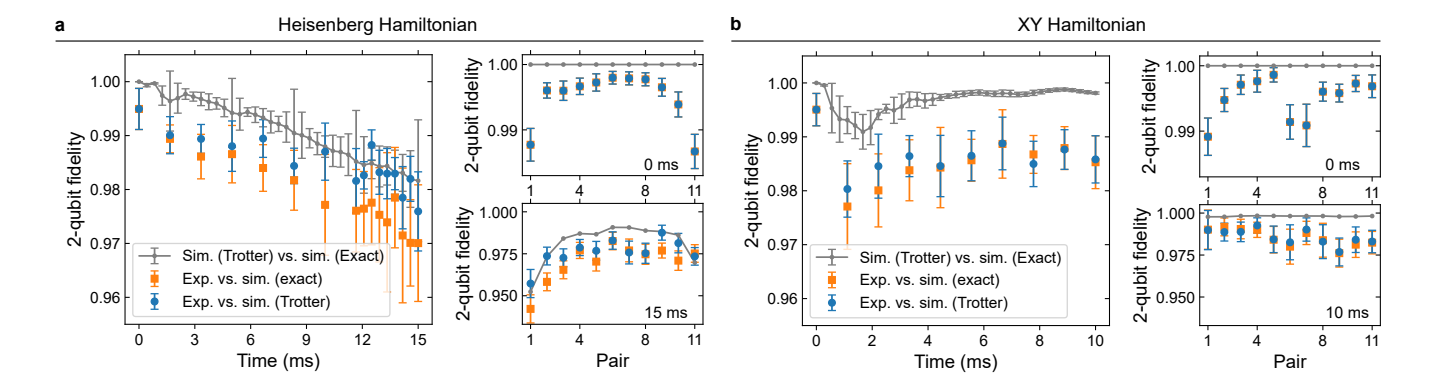


FIG. 6: Measured fidelity of the state resulting from the Trotter approximation: The experimentally observed fidelity, averaged over the ion pairs, is shown across the evolution. Error bars indicate the standard deviation over the pairs. The smaller subplots show the fidelity, at the evolution's start and end, from individual ion pairs' actual states to their ideal states. The measurements were carried out (a) for the Trotter-approximated Heisenberg Hamiltonian and (b) for the Trotter-approximated XY Hamiltonian.

REFERENCES

- [1] T. Fukuhara, P. Schauß, M. Endres, S. Hild, M. Cheneau, I. Bloch, and C. Gross, Microscopic observation of magnon bound states and their dynamics, Nature **502**, 76 (2013).
- [2] J.-Y. Choi, S. Hild, J. Zeiher, P. Schauß, A. Rubio-Abadal, T. Yefsah, V. Khemani, D. A. Huse, I. Bloch, and C. Gross, Exploring the many-body localization transition in two dimensions, Science 352, 1547 (2016).
- [3] J. G. Bohnet, B. C. Sawyer, J. W. Britton, M. L. Wall, A. M. Rey, M. Foss-Feig, and J. J. Bollinger, Quantum spin dynamics and entanglement generation with hundreds of trapped ions, Science 352, 1297 (2016).
- [4] J. Zhang, G. Pagano, P. W. Hess, A. Kyprianidis, P. Becker, H. Kaplan, A. V. Gorshkov, Z.-X. Gong, and C. Monroe, Observation of a many-body dynamical phase transition with a 53-qubit quantum simulator, Nature **551**, 601 (2017).
- [5] M. K. Joshi, F. Kranzl, A. Schuckert, I. Lovas, C. Maier, R. Blatt, M. Knap, and C. F. Roos, Observing emergent hydrodynamics in a long-range quantum magnet, arXiv:2107.00033 (2021).
- [6] P. Scholl, M. Schuler, H. J. Williams, A. A. Eberharter, D. Barredo, K.-N. Schymik, V. Lienhard, L.-P. Henry, T. C. Lang, T. Lahaye, A. M. Läuchli, and A. Browaeys, Quantum simulation of 2d antiferromagnets with hundreds of rydberg atoms, Nature 595, 233 (2021).
- [7] G. Semeghini, H. Levine, A. Keesling, S. Ebadi, T. T. Wang, D. Bluvstein, R. Verresen, H. Pichler, M. Kalinowski, R. Samajdar, A. Omran, S. Sachdev, A. Vishwanath, M. Greiner, V. Vuletic, and M. D. Lukin, Probing topological spin liquids on a programmable quantum simulator, arXiv:2104.04119 (2021).
- [8] F. Kranzl, M. K. Joshi, C. Maier, T. Brydges, J. Franke, R. Blatt, and C. F. Roos, Controlling long ion strings for quantum simulation and precision measurements, arXiv:2112.10655 (2021).
- [9] D. Bluvstein, H. Levine, G. Semeghini, T. T. Wang, S. Ebadi, M. Kalinowski, A. Keesling, N. Maskara, H. Pichler,
 M. Greiner, et al., A quantum processor based on coherent transport of entangled atom arrays, arXiv:2112.03923 (2021).
- [10] A. M. Kaufman, M. E. Tai, A. Lukin, M. Rispoli, R. Schittko, P. M. Preiss, and M. Greiner, Quantum thermalization through entanglement in an isolated many-body system, Science **353**, 794 (2016).
- [11] C. Neill, P. Roushan, M. Fang, Y. Chen, M. Kolodrubetz, Z. Chen, A. Megrant, R. Barends, B. Campbell, B. Chiaro, A. Dunsworth, E. Jeffrey, J. Kelly, J. Mutus, P. J. J. O'Malley, C. Quintana, D. Sank, A. Vainsencher, J. Wenner, T. C. White, A. Polkovnikov, and J. M. Martinis, Ergodic dynamics and thermalization in an isolated quantum system, Nature Physics 12, 1037 (2016).
- [12] G. Clos, D. Porras, U. Warring, and T. Schaetz, Time-resolved observation of thermalization in an isolated quantum system, Phys. Rev. Lett. 117, 170401 (2016).
- [13] J. Goold, M. Huber, A. Riera, L. del Rio, and P. Skrzypczyk, The role of quantum information in thermodynamics—a topical review, Journal of Physics A 49, 143001 (2016).
- [14] S. Vinjanampathy and J. Anders, Quantum thermodynamics, Contemporary Physics 57, 545 (2016).
- [15] E. T. Jaynes, Information Theory and Statistical Mechanics II, Phys. Rev. 108, 171 (1957).
- [16] R. Balian and N. L. Balazs, Equiprobability, inference, and entropy in quantum theory, Annals of Physics 179, 97 (1987).
- [17] M. Lostaglio, The resource theory of quantum thermodynamics, Master's thesis, Imperial College London (2014).
- [18] N. Yunger Halpern, Beyond heat baths ii: framework for generalized thermodynamic resource theories, Journal of Physics A: Mathematical and Theoretical 51, 094001 (2018).
- [19] N. Yunger Halpern, P. Faist, J. Oppenheim, and A. Winter, Microcanonical and resource-theoretic derivations of the thermal state of a quantum system with noncommuting charges, Nature Commun. 7, 12051 (2016).

- [20] Y. Guryanova, S. Popescu, A. J. Short, R. Silva, and P. Skrzypczyk, Thermodynamics of quantum systems with multiple conserved quantities, Nature Commun. 7, 12049 (2016).
- [21] M. Lostaglio, D. Jennings, and T. Rudolph, Thermodynamic resource theories, non-commutativity and maximum entropy principles, New Journal of Physics 19, 043008 (2017).
- [22] N. Yunger Halpern, M. E. Beverland, and A. Kalev, Noncommuting conserved charges in quantum many-body thermalization, Phys. Rev. E 101, 042117 (2020).
- [23] C. Sparaciari, L. Del Rio, C. M. Scandolo, P. Faist, and J. Oppenheim, The first law of general quantum resource theories, Quantum 4, 259 (2020).
- [24] Z. B. Khanian, From quantum source compression to quantum thermodynamics, arXiv:2012.14143 (2020).
- [25] Z. B. Khanian, M. N. Bera, A. Riera, M. Lewenstein, and A. Winter, Resource theory of heat and work with non-commuting charges: yet another new foundation of thermodynamics, arXiv:2011.08020 (2020).
- [26] G. Gour, D. Jennings, F. Buscemi, R. Duan, and I. Marvian, Quantum majorization and a complete set of entropic conditions for quantum thermodynamics, Nature Commun. 9, 5352 (2018).
- [27] G. Manzano, J. M. Parrondo, and G. T. Landi, Non-abelian quantum transport and thermosqueezing effects, arXiv:2011.04560 (2020).
- [28] S. Popescu, A. B. Sainz, A. J. Short, and A. Winter, Quantum reference frames and their applications to thermodynamics, Philosophical Transactions of the Royal Society A: Mathematical, Physical and Engineering Sciences 376, 20180111 (2018).
- [29] S. Popescu, A. B. Sainz, A. J. Short, and A. Winter, Reference frames which separately store noncommuting conserved quantities, Physical Review Letters 125, 090601 (2020).
- [30] K. Ito and M. Hayashi, Optimal performance of generalized heat engines with finite-size baths of arbitrary multiple conserved quantities beyond independent-and-identical-distribution scaling, Phys. Rev. E 97, 012129 (2018).
- [31] M. N. Bera, A. Riera, M. Lewenstein, Z. B. Khanian, and A. Winter, Thermodynamics as a consequence of information conservation, Quantum 3, 121 (2019).
- [32] J. Mur-Petit, A. Relaño, R. A. Molina, and D. Jaksch, Revealing missing charges with generalised quantum fluctuation relations, Nature Commun. 9, 2006 (2018).
- [33] G. Manzano, Squeezed thermal reservoir as a generalized equilibrium reservoir, Physical Review E 98, 042123 (2018).
- [34] G. Manzano, R. Sánchez, R. Silva, G. Haack, J. B. Brask, N. Brunner, and P. P. Potts, Hybrid thermal machines: Generalized thermodynamic resources for multitasking, Physical Review Research 2, 043302 (2020).
- [35] K. Fukai, Y. Nozawa, K. Kawahara, and T. N. Ikeda, Noncommutative generalized gibbs ensemble in isolated integrable quantum systems, Physical Review Research 2, 033403 (2020).
- [36] J. Mur-Petit, A. Relaño, R. A. Molina, and D. Jaksch, Fluctuations of work in realistic equilibrium states of quantum systems with conserved quantities, arXiv:1910.11000 (2019).
- [37] M. Scandi and M. Perarnau-Llobet, Thermodynamic length in open quantum systems, Quantum 3, 197 (2019).
- [38] P. Boes, H. Wilming, J. Eisert, and R. Gallego, Statistical ensembles without typicality, Nature Commun. 9, 1 (2018).
- [39] Y. Mitsuhashi, K. Kaneko, and T. Sagawa, Characterizing symmetry-protected thermal equilibrium by work extraction, arXiv:2103.06060 (2021).
- [40] T. Croucher, J. Wright, A. R. R. Carvalho, S. M. Barnett, and J. A. Vaccaro, Information erasure, in *Thermodynamics in the Quantum Regime: Fundamental Aspects and New Directions*, edited by F. Binder, L. A. Correa, C. Gogolin, J. Anders, and G. Adesso (Springer International Publishing, Cham, 2018) pp. 713–730.
- [41] J. A. Vaccaro and S. M. Barnett, Information erasure without an energy cost, Proceedings of the Royal Society of London A: Mathematical, Physical and Engineering Sciences 467, 1770 (2011).
- [42] J. S. S. T. Wright, T. Gould, A. R. R. Carvalho, S. Bedkihal, and J. A. Vaccaro, Quantum heat engine operating between thermal and spin reservoirs, Phys. Rev. A 97, 052104 (2018).
- [43] N. Yunger Halpern and S. Majidy, How to build hamiltonians that transport noncommuting charges in quantum thermodynamics, npj Quantum Information 8, 10 (2022).
- [44] T. Croucher and J. A. Vaccaro, Memory erasure with finite-sized spin reservoir, arXiv:2111.10930 (2021).
- [45] I. Marvian, H. Liu, and A. Hulse, Qudit circuits with SU(d) symmetry: Locality imposes additional conservation laws, arXiv:2105.12877 (2021).
- [46] I. Marvian, H. Liu, and A. Hulse, Rotationally-Invariant Circuits: Universality with the exchange interaction and two ancilla qubits, arXiv:2202.01963 (2022).
- [47] M. Rigol, Breakdown of thermalization in finite one-dimensional systems, Phys. Rev. Lett. 103, 100403 (2009).
- [48] M. Rigol, V. Dunjko, V. Yurovsky, and M. Olshanii, Relaxation in a completely integrable many-body quantum system: An Ab Initio study of the dynamics of the highly excited states of 1d lattice hard-core bosons, Phys. Rev. Lett. 98, 050405 (2007).
- [49] L. Vidmar and M. Rigol, Generalized gibbs ensemble in integrable lattice models, Journal of Statistical Mechanics: Theory and Experiment 2016, 064007 (2016).
- [50] L. Viola, S. Lloyd, and E. Knill, Universal control of decoupled quantum systems, Phys. Rev. Lett. 83, 4888 (1999).
- [51] E. Jané, G. Vidal, W. Dür, P. Zoller, and J. I. Cirac, Simulation of quantum dynamics with quantum optical systems, Quantum Information and Computation 3, 15 (2003).
- [52] B. P. Lanyon, C. Hempel, D. Nigg, M. Müller, R. Gerritsma, F. Zähringer, P. Schindler, J. T. Barreiro, M. Rambach, G. Kirchmair, M. Hennrich, P. Zoller, R. Blatt, and C. F. Roos, Universal digital quantum simulations with trapped ions, Science 334, 57 (2011).
- [53] Y. Salathé, M. Mondal, M. Oppliger, J. Heinsoo, P. Kurpiers, A. Potočnik, A. Mezzacapo, U. Las Heras, L. Lamata, E. Solano, S. Filipp, and A. Wallraff, Digital quantum simulation of spin models with circuit quantum electrodynamics,

- Phys. Rev. X 5, 021027 (2015).
- [54] S. Geier, N. Thaicharoen, C. Hainaut, T. Franz, A. Salzinger, A. Tebben, D. Grimshandl, G. Zürn, and M. Weidemüller, Floquet hamiltonian engineering of an isolated many-body spin system, Science 374, 1149 (2021).
- [55] P. Scholl, H. J. Williams, G. Bornet, F. Wallner, D. Barredo, T. Lahaye, A. Browaeys, L. Henriet, A. Signoles, C. Hainaut, T. Franz, S. Geier, A. Tebben, A. Salzinger, G. Zürn, and M. Weidemüller, Microwave-engineering of programmable XXZ Hamiltonians in arrays of Rydberg atoms, arXiv:2107.14459 (2021).
- [56] D. Huse, private communication (2021).
- [57] F. Monteiro, M. Tezuka, A. Altland, D. A. Huse, and T. Micklitz, Quantum ergodicity in the many-body localization problem, Phys. Rev. Lett. 127, 030601 (2021).
- [58] T. Langen, S. Erne, R. Geiger, B. Rauer, T. Schweigler, M. Kuhnert, W. Rohringer, I. E. Mazets, T. Gasenzer, and J. Schmiedmayer, Experimental observation of a generalized Gibbs ensemble, Science 348, 207 (2015).
- [59] D. Porras and J. I. Cirac, Effective quantum spin systems with trapped ions, Phys. Rev. Lett. 92, 207901 (2004).
- [60] N. Agmon, Y. Alhassid, and R. Levine, An algorithm for finding the distribution of maximal entropy, Journal of Computational Physics 30, 250 (1979).
- [61] Y. Alhassid, N. Agmon, and R. Levine, An upper bound for the entropy and its applications to the maximal entropy problem, Chemical Physics Letters 53, 22 (1978).
- [62] B. Efron and R. Tibshirani, Bootstrap methods for standard errors, confidence intervals, and other measures of statistical accuracy, Statistical Science 1, 54 (1986).
- [63] W. Beugeling, R. Moessner, and M. Haque, Finite-size scaling of eigenstate thermalization, Phys. Rev. E 89, 042112 (2014).
- [64] Á. L. Corps and A. Relaño, Long-range level correlations in quantum systems with finite hilbert space dimension, Phys. Rev. E 103, 012208 (2021).
- [65] S. Birnkammer, A. Bohrdt, F. Grusdt, and M. Knap, Characterizing topological excitations of a long-range heisenberg model with trapped ions, arXiv:2012.09185 (2020).
- [66] M. K. Joshi, A. Fabre, C. Maier, T. Brydges, D. Kiesenhofer, H. Hainzer, R. Blatt, and C. F. Roos, Polarization-gradient cooling of 1d and 2d ion coulomb crystals, New. J. Phys. 22, 103013 (2020).
- [67] P. Jurcevic, B. P. Lanyon, P. Hauke, C. Hempel, P. Zoller, R. Blatt, and C. F. Roos, Quasiparticle engineering and entanglement propagation in a quantum many-body system, Nature 511, 202 (2014).
- [68] T. Graß and M. Lewenstein, Trapped-ion quantum simulation of tunable-range Heisenberg chains, EPJ Quantum Technology 1, 8 (2014).
- [69] S. Lloyd, Universal quantum simulators, Science 273, 1073 (1996).
- [70] T. Brydges, A. Elben, P. Jurcevic, B. Vermersch, C. Maier, B. P. Lanyon, P. Zoller, R. Blatt, and C. F. Roos, Probing rényi entanglement entropy via randomized measurements, Science 364, 260 (2019).
- [71] M. Ježek, J. Fiurášek, and Z. c. v. Hradil, Quantum inference of states and processes, Phys. Rev. A 68, 012305 (2003).
- [72] M. M. Wilde, From Classical to Quantum Shannon Theory, arXiv:1106.1445 (2011).